Mixed-order semiclassical dynamics in coherent state representation: The connection between phonon sidebands and guest–host dynamics

M. Ovchinnikov and V. A. Apkarian
Department of Chemistry, University of California, Irvine, California 92697-2025

(Received 3 September 1997; accepted 29 October 1997)

The formalism of mixed-order semiclassical molecular dynamics in coherent state representation is developed and applied to calculations of quantum time correlation functions in extended systems. The method allows the consistent treatment of a selected number of degrees of freedom to second order in the stationary phase approximation, through the Herman and Kluk propagator, while the rest of the system is treated to zeroth order, using frozen Gaussians. The formulation is applied to calculate the absorption spectrum, of the $B \leftarrow X$ transition of Cl_2 isolated in solid Ar a spectrum that shows zero-phonon lines and phonon sidebands with relative intensities that depend on the excited state vibrational level. The explicit simulation of quantum time correlation functions of the system consisting of 321 degrees of freedom, reproduces the spectrum and allows its interpretation in terms of the underlying molecular motions. Details of the dynamics of a chromophore coupled to lattice phonons are discussed. © *1998 American Institute of Physics.* [S0021-9606(98)50106-7]

I. INTRODUCTION

That spectral observables in condensed media are most naturally treated in terms of time-dependent quantum correlation functions is well recognized. In systems of large dimensionality, due to the large densities of states of relevance, the Franck–Condon analysis of transitions among eigenstates becomes impractical. In contrast, the time-dependent picture leads to compact notation, and gives a more transparent insight regarding observables. As a corollary, it is more natural to relate spectral features to processes, rather than states. For example, in the case of electronic transitions which concern us in this paper, the absorption spectrum can be thought of as the real part of the Fourier transform of the quantum correlation function, $C(t)$:[1]

$$C(t)=\langle \psi_g(\{q_i\})|e^{-iH_e t/\hbar}|\psi_g(\{q_i\})\rangle, \tag{1}$$

in which $\psi_g(\{q_i\})$ is the initial state wave function of all coordinates $\{q_i\}$, propagated by the excited state Hamiltonian, H_e. Note in Eq. (1) we have neglected the transition dipole function from consideration, a consideration that does not change the conceptual framework of the development.[1] To render a realistic simulation of condensed phase systems, the evaluation of Eq. (1) requires the computation of time-dependent wave functions of hundreds of degrees of freedom. The exact time propagation of quantum Hamiltonians of such large dimensionality is not tractable. However, given that condensed phase spectra commonly relate relatively short time dynamics, semiclassical initial value methods[1–21] may be employed within their limits of validity to provide an accurate, atomistic interpretation of observables. We recently provided such an analysis, in terms of mixed-order semiclassical molecular dynamics in coordinate representation, to analyze absorption emission and resonance Raman spectra,[19] including quantum interferences,[20] of matrix isolated iodine. Here we develop the same concept in coherent state representation, and apply it to the electronic absorption spectrum of Cl_2 isolated in solid Ar.[22] This spectrum shows extensive phonon activity, in the form of excitation dependent phonon sidebands, and our analysis allows a direct dissection of the molecular mechanics underlying the spectrum.

There has been considerable recent interest in applications of semiclassical initial value methods to problems in chemical dynamics. The core of such treatments rely on the use of the Van Vleck propagator,[23] which approximates the quantum time propagator to second order in stationary phase, and can be rigorously developed in various representations as shown by Gutzwiller.[24] The most widely used version of these trajectory based methods is the Herman and Kluk (HK) propagator,[3] which develops in the coherent representation of Gaussian bases, and was devised as a refinement of Heller's frozen Gaussian approximation (FGA),[4] by demanding proper asymptotic behavior in the limit $\hbar \rightarrow 0$. Various implementations of the HK propagator have been demonstrated in applications ranging from model bound state and photodissociation problems,[2–9] to spectral analysis,[7–9] to cumulative reaction probabilities,[10] to transition state resonances,[11] to tunneling,[10,12,13] and nonadiabatic dynamics.[14–16] These studies are limited to two- or three-dimensional systems, devised for rigorous tests of the utility of these classical trajectory-based methods in reproducing quantum expectation values. In that respect, perhaps one of the more rigorous tests is the case of ''deep'' tunneling dynamics, which has been demonstrated to be fully retrievable at least in the tested case of a one-dimensional Ekhart potential.[13] Although the unique advantage of semiclassical initial value methods in treating systems of large dimensionality has been recognized, and methods have been formally developed and suggested,[17,18] beside our work[19,20] the only such example is that of Brewer *et al.*[21] who simulated the photodetachment spectra of Ar_nI^- with up to 15 coupled degrees of freedom. Their particular implementation, in terms of the cellularized frozen Gaussian approximation

(CFGA), propagates all degrees of freedom equivalently,[21] through the HK propagator, and constructs correlations using the cellular dynamics algorithm of Heller.[5]

We are interested in the explicit treatment of hundreds of degrees of freedom in which the uniform second-order propagation of all coordinates is neither practical nor necessary. We have previously shown through model calculations that a consistent treatment of large systems is possible by dividing coordinates according to their thermal occupation, reserving the second-order propagation to coordinates of low thermal occupancy while treating the rest with the zeroth-order propagator.[19] This general strategy was also suggested by Sun and Miller in their contemporaneous work.[18] Note, in coordinate representation, zeroth-order propagation simply implies the calculation of classical trajectories and weighting them by the action accumulated along the classical path. Since classical trajectories represent delta functions in phase space, the construction of correlation functions from such swarms requires some thought, and we suggested the use of the initial thermal density matrix for this purpose.[19] Such considerations do not arise when using coherent bases in the propagation. As we expand below, in the present, we achieve a consistent mixed-order treatment by the combination of HK and FGA propagators which can be extended to initial states at 0 K. Further, in contrast with delta functions, the Gaussian basis has the advantage of a significantly more efficient sampling of systems of large dimensionality, allowing a statistically reliable representation of time-dependent wave functions with a finite number of trajectories.

II. METHOD

The HK propagator is the initial value Van Vleck propagator given in the coherent representation of Gaussian bases. The $|\mathbf{p},\mathbf{q}\rangle$ basis functions of the n-dimensional coordinate space $\mathbf{x}=(x_1,x_2,\ldots,x_n)$ are defined as

$$\langle \mathbf{p},\mathbf{q}|\mathbf{x}\rangle = e^{-\gamma(\mathbf{x}-\mathbf{q})^2} e^{(i/\hbar)\mathbf{p}(\mathbf{x}-\mathbf{q})}, \tag{2}$$

the states are Gaussian in both coordinate and momentum space, centered at vectors $\mathbf{p}$ and $\mathbf{q}$, with the vector $\gamma=(\gamma_1,\gamma_2,\ldots,\gamma_n)$ defining the Gaussian widths. The HK time propagator is given by

$$e^{(i/\hbar)\hat{H}t} = \int d^n\mathbf{p}_0 d^n\mathbf{q}_0 |\mathbf{p}_t,\mathbf{q}_t\rangle J(\mathbf{p}_0,\mathbf{q}_0,t) e^{(i/\hbar)S(\mathbf{p}_0,\mathbf{q}_0,t)} \times \langle \mathbf{p}_0,\mathbf{q}_0|, \tag{3}$$

where the integral is performed over the initial conditions of the trajectories $\mathbf{p}_0$, $\mathbf{q}_0$; the phase space coordinates of the classical trajectories after time t are given as $\mathbf{p}_t$, $\mathbf{q}_t$; $S(\mathbf{p}_0,\mathbf{q}_0,t)$ is the action along the classical path; and $J(\mathbf{p}_0,\mathbf{q}_0,t)$ is the weight of a trajectory that defines its contribution to the overall wave function. The computationally intense part of the implementation is the evaluation of the weights of trajectories, which are obtained through time-dependent monodromy (stability) matrices:

$$J(t) = \left\{ \det\left[\frac{1}{2}\left(\mathbf{M}_{pp} + \mathbf{M}_{qq} - 2i\gamma\hbar \mathbf{M}_{qp} + \frac{i}{2\gamma\hbar}\mathbf{M}_{pq} \right) \right] \right\}^{1/2}, \tag{4}$$

where the matrices are defined along the trajectories as

$$\mathbf{M}_{qq} = \frac{d\mathbf{q}_t}{d\mathbf{q}_0}, \quad \mathbf{M}_{pp} = \frac{d\mathbf{p}_t}{d\mathbf{p}_0}, \quad \mathbf{M}_{qp} = \frac{d\mathbf{q}_t}{d\mathbf{p}_0}, \quad \mathbf{M}_{pq} = \frac{d\mathbf{p}_t}{d\mathbf{q}_0} \tag{5}$$

and measure the sensitivity of final momentum and position with respect to their initial choices. The calculation of the stability matrices involves the solution of N^2 coupled equations of motion:

$$\frac{d}{dt}\mathbf{M}_{pp} = -\mathbf{V}_{qq}(\mathbf{p}_0,\mathbf{q}_0,t)\mathbf{M}_{qp}, \tag{6a}$$

$$\frac{d}{dt}\mathbf{M}_{pq} = -\mathbf{V}_{qq}(\mathbf{p}_0,\mathbf{q}_0,t)\mathbf{M}_{qq}, \tag{6b}$$

$$\frac{d}{dt}\mathbf{M}_{qp} = \frac{1}{m}\mathbf{M}_{pp}, \tag{6c}$$

$$\frac{d}{dt}\mathbf{M}_{qq} = \frac{1}{m}\mathbf{M}_{pq}, \tag{6d}$$

with initial conditions, $\mathbf{M}_{qq}=1$, $\mathbf{M}_{qp}=0$, $\mathbf{M}_{pq}=0$, $\mathbf{M}_{pp}=1$; and where $\mathbf{V}_{qq}(\mathbf{p}_0,\mathbf{q}_0,t)$ is the Hessian matrix of second derivatives of the potential with respect to coordinates calculated at position $\mathbf{q}_t$.

The initial conditions for integration of the HK propagator is accomplished through Monte Carlo sampling of the quantum wave function by Gaussians, the statistics of which is the single most important consideration in reaching convergence by this method. Proper sampling is ensured by demanding that the contribution to the integral be approximately equal for each of the trajectories. For example, if one is interested in the correlation function $C(t)=\langle\psi(t)|\psi(0)\rangle$ which arises in linear spectroscopy, the required algorithm can be expressed as

$$\begin{aligned} C(t) &= \int d''\mathbf{p}_0 d''\mathbf{q}_0 \langle\psi_0|\mathbf{p}_t,\mathbf{q}_t\rangle J(\mathbf{p}_0,\mathbf{q}_0,t) e^{(i/\hbar)S(\mathbf{p}_0,\mathbf{q}_0,t)} \times \langle \mathbf{p}_0,\mathbf{q}_0|\psi_0\rangle \\ &= \sum_{\rho(\mathbf{p}_0,\mathbf{q}_0)=|\langle \mathbf{p}_0,\mathbf{q}_0|\psi_0\rangle|^2} J(\mathbf{p}_0,\mathbf{q}_0,t) e^{(i/\hbar)S(\mathbf{p}_0,\mathbf{q}_0,t)} \times \frac{\langle\psi_0|\mathbf{p}_t,\mathbf{q}_t\rangle}{\langle\psi_0|\mathbf{p}_0,\mathbf{q}_0\rangle}. \end{aligned} \tag{7}$$

While this gives perfect sampling at $t=0$, as time progresses, the magnitudes of the weights of the trajectories $|J(t)|$ grow exponentially at a rate determined by the extent of the anharmonicity in the system, and compromises the statistics. This can be understood by noting that the wave function at a point $\mathbf{x}$ is given as a statistical sum over all contributing trajectories, then the statistical error due to this sampling can be estimated to vary as $\Delta\psi \propto \langle |J(t)| \rangle N^{1/2}$, where N is the num-

ber of contributing trajectories. At $t=0$, the magnitudes of weights are unity. As time progresses, the method breaks down due to the exponential growth of $|J(t)|$ when the error becomes comparable to the wave function itself. If $|J(t)|$ increases tenfold for a given trajectory, then the number of trajectories must be increased by a factor of one-hundred, to maintain the original statistical error. This constitutes the main limitation of the HK propagator in multidimensional systems, and for long propagation times. The value of $|J(t)|$ provides an internal indicator for nonconvergence.

For multidimensional systems, it is advantageous to propagate dynamics in the coordinates of normal vibrational modes, as opposed to Cartesian coordinates commonly used in MD simulations. In our particular application, simulations in a solid at cryogenic temperature, the initial motions of the majority of degrees of freedom are nearly harmonic. It is therefore natural to choose mass weighted normal vibrational modes of the ground electronic surface as the principle coordinates. This allows the choice of the Gaussian widths to correspond to those of the zero-point vibrational wave function:

$$\gamma_i=\frac{\omega_i}{2\hbar}. \tag{8}$$

It is easy to verify, using Eq. (6), that the weight corresponding to propagation of such Gaussians in one-dimensional harmonic potentials equals 1. The initial wave function in Eq. (2) is then described by the zero coordinate-momentum coherent state:

$$\psi_0=|\mathbf{0},\mathbf{0}\rangle=|0,0;0,0;\ldots;0,0\rangle. \tag{9}$$

The normal-mode coordinates also provide criteria for subdividing the system into modes to be propagated to second order and zeroth order, through the HK and FGA propagators, respectively. Only for the sake of convenience we will refer to these as system and bath coordinates, otherwise, we emphasize that any of the coordinates may be involved in the subgrouping. Indeed, the extent of anharmonicity or the extent of coupling to the chromophore, may be more meaningful criteria for the subdivision, and in practice it is easier to make decisions after an initial run. Choosing n degrees of freedom as system, and the rest N-n degrees of freedom as bath, correlation functions can be devised as

$$\begin{aligned}C(t)&=\int\prod_{i=1}^{N}dp_{i,0}dq_{i,0}\langle\mathbf{0},\mathbf{0}|\mathbf{p}_t,\mathbf{q}_t\rangle J(\mathbf{p}_0,\mathbf{q}_0,t)e^{(i/\hbar)S(\mathbf{p}_0,\mathbf{q}_0,t)}\\&\quad\times\langle\mathbf{p}_0,\mathbf{q}_0|\mathbf{0},\mathbf{0}\rangle\\&=\int\prod_{i=1}^{n}dp_{i,0}dq_{i,0}\langle\mathbf{0},\mathbf{0}|\mathbf{p}_t,\mathbf{q}_t\rangle\\&\quad\times J_{\mathrm{sys}}(\mathbf{p}_0,\mathbf{q}_0,t)e^{(i/\hbar)S(\mathbf{p}_0,\mathbf{q}_0,t)}{}_{\mathrm{bath}}\langle\mathbf{0},\mathbf{0}|_{\mathrm{sys}}\langle\mathbf{p}_0,\mathbf{q}_0|\mathbf{0},\mathbf{0}\rangle.\end{aligned} \tag{10}$$

The sampling of the Gaussians (the integration) is done in n-dimensional space; and the weights J_{sys} are calculated from the $n\times n$ blocks of the total monodromy matrices. For the rest of the N-n degrees of freedom, the initial conditions for the Gaussians are taken to be **0,0** with no contribution to the weights from their propagation. The above accomplishes the mixed-order propagation, HK for the system degrees of freedom while using Heller's original frozen Gaussians for the bath degrees of freedom, where the widths of all Gaussians correspond exactly to the zero vibrational wave function in each mode. Note, however, the molecular dynamics is propagated in the full multidimensional space: all degrees of freedom are coupled and no assumption of separability is made.

The HK propagator, Eq. (3), is exact for coupled harmonic oscillators, and remains a good approximation for a limited time for anharmonic oscillators. To the extent that the HK propagator describes the system, the propagator in Eq. (10) is exact for a system linearly coupled to a harmonic bath, for Hamiltonians of the form:

$$H=H_{\mathrm{sys}}+\sum_i\left\{\frac{1}{2}p_i^2+\frac{\omega_i^2}{2}q_i^2+[f_i(q_{\mathrm{sys}})]q_i\right\}. \tag{11}$$

Note that in this implied separation of degrees of freedom, the characteristic frequencies of the system are much higher than those of the bath. Then, where the mean-field approximation of the coupling by its time average $[f_i(q_{\mathrm{sys}})]=\langle f_i\rangle$, is applicable, Eq. (10) becomes rigorously exact.

III. SYSTEM AND IMPLEMENTATION

The target spectrum for this implementation is the $B\leftarrow X$ transition of molecular chlorine isolated in solid Ar.[22] While this same transition in the case of iodine shows no structure, and was the subject of our prior analysis,[19] in the case of Cl_2 the spectrum is composed of sharp zero-phonon lines, accompanied by phonon sidebands to the blue of each. The relative intensity of zero-phonon and phonon sideband depends on the Cl_2 vibrational quantum number in the upper state. Near the origin of the transition, near $v=2$, the sideband is imperceptible. Near the dissociation limit the zero-phonon lines blend into the continuum of sidebands, and can no longer be identified. Quite clearly the coupling between the chromophore and the lattice is dynamical in nature, not the result of the difference between excited and ground-state Cl–Ar potentials. To further concentrate on this purely dynamical activation of sidebands, in our treatment we will assume the same Ar–Cl potentials in both X and B states of the molecule; further, we will assume that the same pairwise additive Lennard–Jones potentials ($\sigma=3.41$ Å, $\varepsilon=116.4$ K) describe both Ar–Ar and Cl–Ar interactions. The ground and excited states of Cl_2 are taken to be Morse functions:

$$V_{\mathrm{Cl-Cl}}=D_e[1-\exp(-\beta(r-r_e))]^2 \tag{12}$$

with parameters $D_e=25\,500\ \mathrm{cm}^{-1}$, $\beta=1.947\ \text{Å}^{-1}$, and $r_e=1.988$ Å in the ground X state, and $D_e=3145\ \mathrm{cm}^{-1}$, $\beta=2.39\ \text{Å}^{-1}$, and $r_e=2.396$ Å in the excited B state.[25] We reemphasize that the only difference between excited and ground electronic states of our system is due to the difference in the Cl_2 potential, all other interactions being the same.

In the simulations the Cl_2 molecule is inserted into a double substitutional site of $3\times3\times3$ unit cells of Ar, by replacing a nearest-neighbor pair of Ar atoms with molecular Cl_2. The simulation box is treated subject to periodic bound-

ary conditions. The minimum potential-energy configuration of the doped lattice is determined via Monte Carlo simulated annealing, and the lattice constant is adjusted for 0 pressure. The choice of the double substitutional site is justified experimentally, based on vuv spectroscopy of Cl atoms after photodissociation of Cl_2 in Ar.[26] This choice is also consistent with energetic considerations.[27] We verify that the minimization of the Cl_2/Ar_{107} system, in comparison to Cl_2/Ar_{106}, shows that the energy gain is less than that of the cohesive energy of an Ar atom.

Once the potential energy is minimized, the vibrational normal modes are determined by diagonalization of the matrix:

$$A_{ij}=\frac{1}{\sqrt{m_i m_j}}\frac{\partial^2 V(x)}{\partial x_i \partial x_j}. \tag{13}$$

The resulting density of states of the doped solid and that of the neat Ar_{108} cell are shown in Fig. 1, along with the bulk density of states.[28] In the finite system, the tail of the acoustic phonon distribution is absent, the lowest acoustic phonon frequency of the undoped cell being 19 cm^{-1}. The insertion of Cl_2 in the solid breaks the degeneracies of modes in the pure solid, leading to a broader dispersion of frequencies [note, the ordinates in Figs. 1(a) and 1(b) are different]. In addition, the impurity generates local modes, both high-frequency modes outside the Debye limit and resonant modes within the density of states. The origin of these two different groupings is obvious. The substitution involves the removal of a nearest neighbor pair of Ar atoms with a spacing of 3.762 Å, and replacing them with a Cl_2 molecule with a bond length of 1.988 Å. This creates negative pressure along the molecular axis due to the loose fit, and high pressure perpendicular to it, all modes involving motion along the molecular axis are softened while modes involving motion perpendicular to the molecular axis are stiffened. The lowest-frequency mode in the doped solid is now at 12 cm^{-1}, and involves motion of the molecular center of mass along the molecular axis.

The system dynamics is propagated in normal-mode coordinates; while the potential energy, forces, and the Hessian are calculated using pair potentials in Cartesian coordinates. The algorithm therefore involves matrix transformation of coordinates at each time step. The numerical algorithm is written with complete generality regarding coordinates to be treated as system or bath.

With the chosen Cl_2 potentials, vertical projection of the $v=0$ wave function of $Cl_2(X)$ onto the B state repulsive wall leads to a very broad absorption spectrum, spanning the range 16 000–27 000 cm^{-1}. The dissociation energy of the B state is ~19 000 cm^{-1}. Consistent with this, the structure in the experimental excitation spectrum is limited to the range 16 000–19 000 cm^{-1}, i.e., is limited to only a small range of the vertically accessible region. Accordingly, if we were to sample the proper ground-state wave function of Cl_2 for our initial distribution, most of the trajectories would contribute to the uninteresting structureless part. To maintain proper statistics in the region of interest, while keeping the size of the trajectory ensemble manageable, we sample from

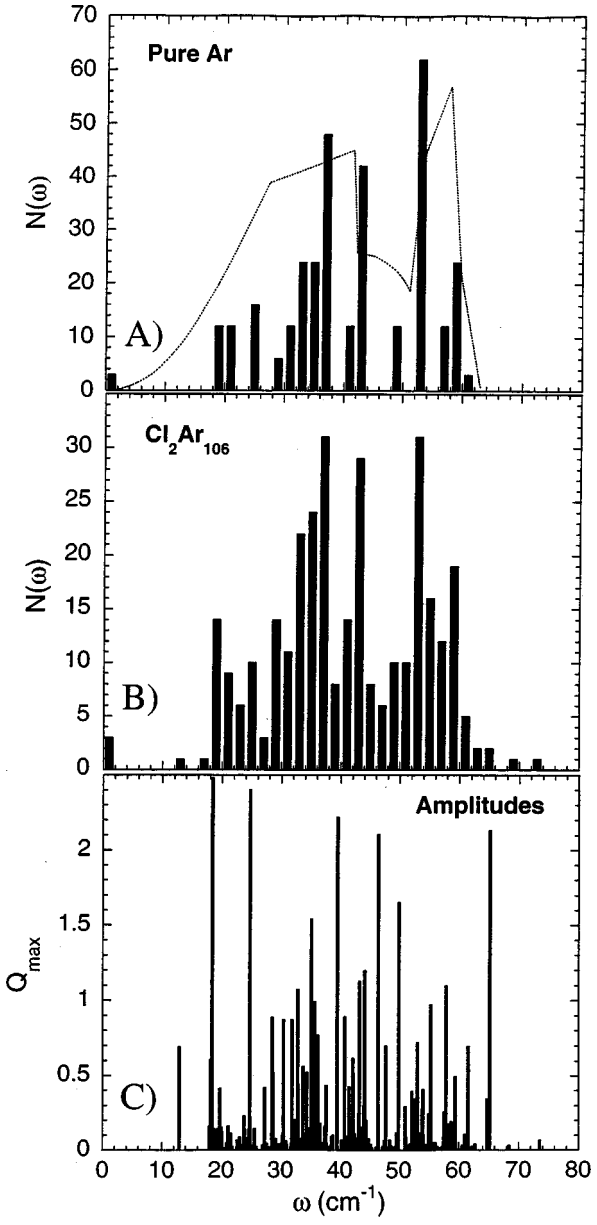

FIG. 1. (a) The density of the vibrational states of the pure Ar_{108} lattice with periodic boundary conditions. The stick spectrum represents the number of vibrational normal modes per 2 cm^{-1} interval. The dashed line is the calculated density of phonon states for bulk Ar (Ref. 28). (b) The density of states for the same lattice doped with Cl_2. (c) The maximum amplitude of the phonons during the 2 ps propagation of the system on the excited electronic potential surface (Cl_2 is in the B electronic state) with initial conditions corresponding to the minimum of the potential energy of the ground state (Cl_2 in the X electronic state).

an artificial initial wave function on Cl_2, a Gaussian centered at 2.17 Å, with a width of $\gamma=72$ $Å^{-2}$. While this choice guarantees vertical access to the structured region of the spectrum, it will clearly not produce the proper Franck–Condon envelope. Note, the published experimental spectrum also suffers from this shortcoming, it is recorded in a limited range and it has not been normalized to the incident laser intensity.[22] In both simulation and experiment the information regarding line shapes and relative intensities of zero-phonon lines and phonon sidebands is reliable.

The most obvious decomposition into system and bath is

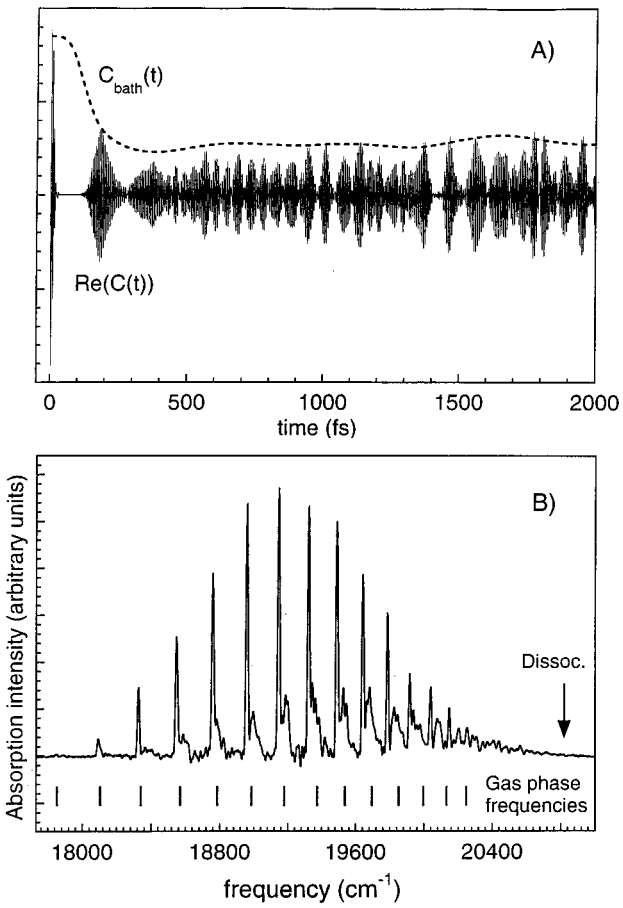

FIG. 2. (a) Real part of the correlation function obtained by running 2000 classical trajectories on the excited state of the system, along with the magnitude of the bath correlation function (see text). (b) Absorption spectrum of the $(B-X)$ transition of Cl_2 in solid Ar calculated by Fourier transformation of the correlation function in (a). The sticks below the spectrum show the vibrational frequencies of the free Cl_2 molecule, shifted by the solvation energy of 70 cm^{-1}. The arrow indicates the dissociation energy of the free molecule.

the choice of the mode involving the Cl_2 internal vibration as system, while the rest of the modes are propagated as bath, i.e., $n=1$. The correlation function shown in Fig. 2(a) is obtained from an ensemble of 2000 trajectories, propagated for 2 ps. This correlation function was compared with that obtained with only 1000 trajectories. While in the first 1 ps the two results are essentially identical (the simulation is converged), near the end of 2 ps, statistical noise of $\sim 10\%$ is observed. Clearly, the Gaussian representation of this 321 -dimensional wave function with only 2000 trajectories is not reliable past 2 ps.

Also provided in Fig. 2(a) is the magnitude of the bath correlation function defined as

$$C(t)_{\text{bath}}=\left|\int d\mathbf{p}_0 d\mathbf{q}_0 \langle \mathbf{0},\mathbf{0}|\mathbf{p}_t,\mathbf{q}_t\rangle_{\text{bath}}\right|, \tag{14}$$

where the integration is over bath coordinates, and which represents the mean response of the bath to the chromophore excitation. This is a measure of the involvement of the lattice motions in the ungoing dynamics. In a mean-field approximation, which is not made in the simulations, the overall

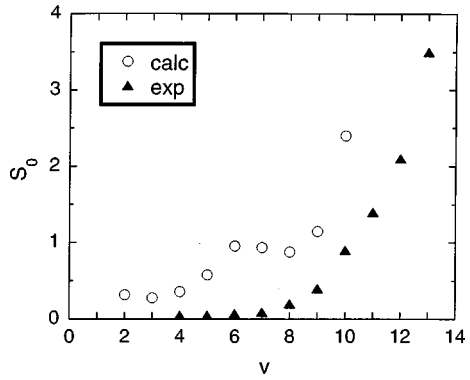

FIG. 3. The ratio of the intensity of the phonon sideband to the intensity of zero-phonon line S_0 as a function of vibrational quantum number. Circles show the result of this work, while triangles are from the experiment (Ref. 22).

correlation function is given as the product of system and bath, $C(t)=C_{\text{sys}}(t)\cdot C_{\text{bath}}(t)$. The fact that the mean bath correlation does not decay to zero during the simulation time implies that recursions will survive to give sharply structured spectral features.

The extent of participation of the different modes in the ongoing dynamics can be discerned from their vibrational amplitudes. This will clearly vary from one trajectory to another, depending on the sampling of initial conditions. A representative analysis is provided by running a single trajectory, starting from the 0,0 coordinate in all degrees of freedom. The maximum amplitudes reached in the course of a 2 ps run in such a trajectory is shown in Fig. 1(c). It can be seen that a large number of modes, spread over the entire spectrum, are coupled to the chromophore excitation and participate to a different extent in the ongoing dynamics. What should be obvious from Fig. 1(c) is that the excitation of the various phonon modes is not spectrally selective, nor can it be broken down in terms of local and bulk phonons. For example, the local modes near 68 cm^{-1} and 74 cm^{-1} are not excited. We will provide an analysis of these motions below.

The spectrum shown in Fig. 2(b) is obtained as the Fourier transform of the correlation function shown in Fig. 2(a) using a Gaussian window: $\exp[-(t/\tau)^2]$, with $\tau=1.4$ ps. The observed zero-phonon linewidths are determined by this window. The spectrum quite closely reproduces the experiment. In particular, the relative intensities of the phonon sidebands to zero-phonon lines, S_0, as a function of vibrational state in $Cl_2(B)$ is well reproduced, as shown in the comparison of Fig. 3. The relative intensity S_0 is a a measure of the dynamical coupling between guest and host degrees of freedom or the electron–phonon coupling strength.[29] Note that, if standard mixed quantum-classical formalisms were used, then a vibration-dependent coupling could not be produced, due to the implicit assumption of separability between quantum and classical degrees of freedom made in such approaches. Quite clearly, no such assumption is made here.

The extent of coupling of a given mode, as judged from the vibrational amplitudes seen in Fig. 1(c), can be used as a criterion to include them in the system partition, to treat them

TABLE I. Vibrational spacings of $Cl_2(B)$ in matrix versus free molecule.

v	Simulation $\Delta G(v)_{\text{matrix}}$[a]	Experiment[b] $\Delta G(v)_{\text{matrix}}$	Theoretical[c] $\Delta G(v)_{\text{free}}$
1	244[d]	⋯	251
2	232	235	240.1
3	222	225	229.2
4	212	217	218.3
5	204	201	207.4
6	183	193	196.5
7	175	184	185.6
8	165	170	174.7
9	158	162	163.8
10	143	150	152.9
11	128	136	142
12	123	129	131.1
13	111	114	120.2
14	104	105	109.3

[a]$\Delta G(v)=G(v)-G(v-1)$, the difference between energies of zero-phonon lines.
[b]From Ref. 22.
[c]Energies based on B state potential assumed in the present simulations (see text).
[d]Values in cm^{-1} units.

by the HK propagator. We carry out a second simulation, now with $n=3$, in which we include the strongly coupled modes at 65.2 and 46.5 cm^{-1} as part of the system. Within the statistical noise, the correlation function obtained from such a simulation, and the associated spectrum, is indistinguishable from the $n=1$ simulation. We conclude that rather than anharmonicity of the bath coordinates, the shear number of them is responsible for not reaching convergence after 2 ps. Thus the more profitable approach for accuracy in this case is the increase of the trajectory ensemble, rather than the partitioning of system and bath. The computational effort, in our present algorithm, increases as $(n^2+1)N^2$. To reduce the statistical noise at the end of the 2 ps propagation to 1%, an ensemble of $\sim$100 000 trajectories is required.

With the satisfactory simulation of the targeted vibronic spectrum in its full dimensionality, we proceed in the next section to a discussion of the information content in such an analysis, and further clarify the nature of the dynamics that justifies the treatment.

IV. DISCUSSION

The vibrational assignments of the simulated zero-phonon lines along with the indication of the positions of the same in the free molecule are indicated in Fig. 2(b). The vibronic origin in the simulation is shifted by 70 cm^{-1}. This shift can be entirely ascribed to solvation of the minimum of the upper state, due to the larger internuclear distance of $Cl_2(B)$. Indeed, when the Cl_2 internuclear distance is fixed at its B state value and the lattice energy is minimized a solvation energy of 72 cm^{-1} is obtained. The experimental shift is 200 cm^{-1}.[22] This discrepancy is not surprising, since in the present we have used isotropic Ar–Ar pair potentials to describe the Cl–Ar interactions in both excited and ground states, which we know to be an inaccurate description of the Cl_2–Ar complex.[30] More interesting are the differences in relative spacings, which are collected in Table I. In the mid-

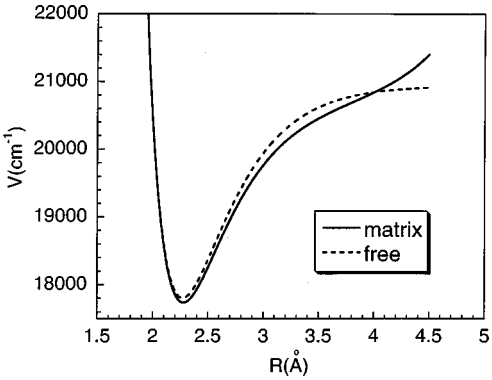

FIG. 4. Sudden excited state potential (solid curve), obtained by stretching the Cl–Cl distance while keeping the lattice at its ground-state equilibrium position, compared to the assumed free molecule potential (dashed curve).

section of the B potential the solid-state spacings are closer than what would be expected based on the free molecule potentials used in the simulations, implying a softer potential. This can be well rationalized by the comparison in Fig. 4, in which the sudden B potential obtained by stretching the Cl–Cl internuclear distance while keeping the lattice at its ground state equilibrium position, is compared with that of the free molecule. When the Cl_2 bond is stretched, initially the molecule experiences attraction from the axial Ar atoms that are held back by the lattice structure. Once the molecular bond length reaches the nearest-neighbor distance of the lattice, the interaction with the axial atoms of the cage becomes repulsive. However, in this range zero-phonon lines cannot be identified, neither in experiment nor in simulations. Thus the vibronic shifts can be mainly understood by the effective potential, a static equilibrium property.

In contrast, and by design, the generation of the phonon sidebands and their relative intensities are strictly dynamical properties. To illustrate this we choose two trajectories from the ensemble for dissection, and plot them along the Cl–Cl coordinate in Fig. 5(a). The trajectory shown with the dashed line starts deep in the B state potential, while the solid trajectory starts near the dissociation limit. The first contributes to the red side of the spectrum, while the second contributes to the continuum on the blue side. We also show the bath correlation functions associated with each of these trajectories. The bath correlation function for an individual trajectory is simply the correlation of the Gaussians projected onto the bath degrees of freedom.

$$C(t)_{\text{bath}}=\langle \mathbf{0},\mathbf{0}|\mathbf{p}_t,\mathbf{q}_t\rangle_{\text{bath}}. \tag{15}$$

For the low-energy trajectory, the bath correlation function decays in the first 200 fs to $\sim$0.7, and stays at this level for the rest of the simulation period. This simply translates to $\sim$70% contribution to the zero-phonon line for this trajectory. In the case of the high-energy trajectory, the bath correlation function decays to nearly zero within $\sim$300 fs, prior to recursions along the Cl–Cl coordinate as can be seen from Fig. 5(a). This trajectory therefore exclusively contributes to the continuous background on the blue side of the spectrum, and does not produce zero-phonon lines. The distinction between the dynamics in these two cases is clear. The large

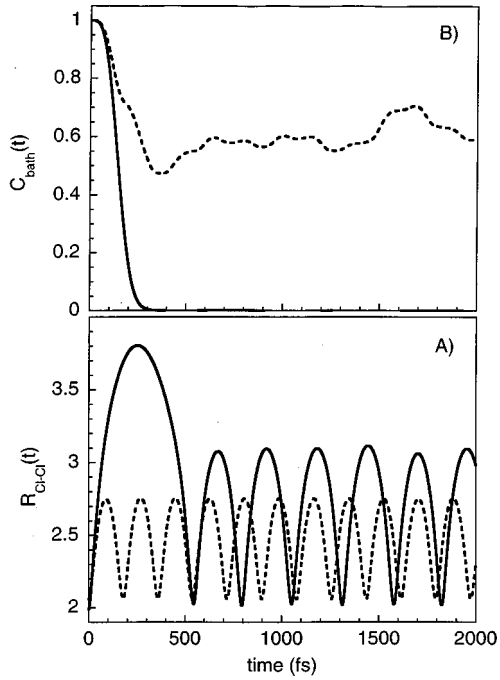

FIG. 5. Two representative trajectories (solid line, at high energy, dashed line, at low energy) chosen from the ensemble of 2000 used for the spectral calculation. The bottom graph shows the time propagation of Cl–Cl internuclear separation. The top graph shows bath correlation functions associated with these trajectories.

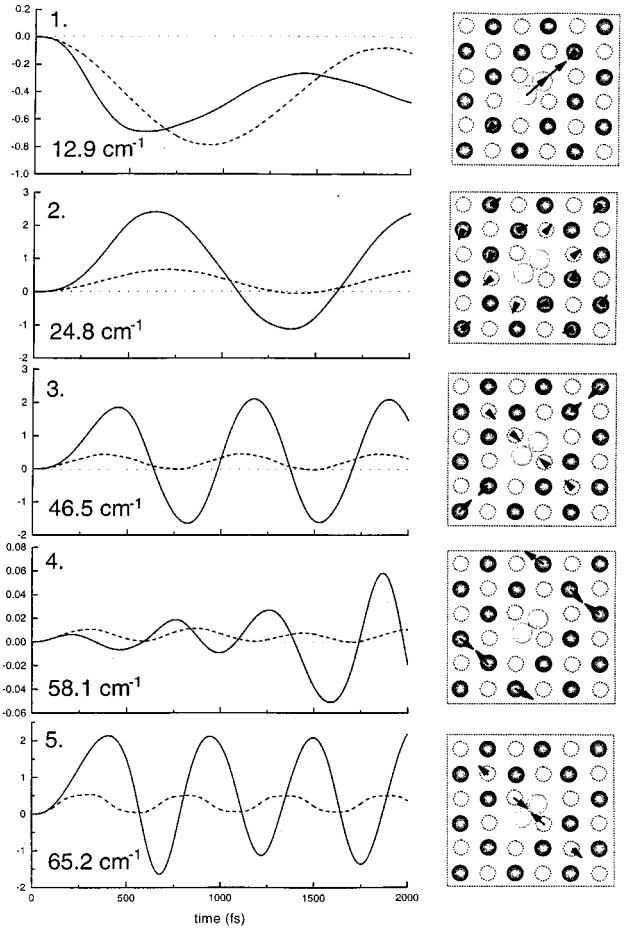

FIG. 6. Representative normal vibrational modes of the system associated with the trajectories of Fig. 5: time-dependent amplitudes are shown in the left panel, while displacement vectors describing the modes are shown in the right panel. Filled circles represent atoms in the plane of the paper, while dashed hollow circles represent atoms a plane below.

amplitude motion in the second case impulsively drives the system, preempting any periodicity in the coherence, or equivalently, any recursions in the collective overlap of the position-momentum bases.

We next investigate representative phonon modes driven by these two trajectories. Such a set is collected in Fig. 6, showing the displacement vectors of each mode on the right panels and the trajectories in the left panels. The low-energy trajectories, shown in dashed lines, are highly harmonic. In fact, in all cases these motions correspond to those of displaced oscillators, in which the potential minima are shifted by some small value from their original positions (the zero line in all cases corresponds to the minimum of the potential energy when Cl_2 is in the X state). The displacement of these oscillators is in response to the shift in the Cl_2 potential minimum of ~ 0.27 Å in the excited state. In this regime, the coupling between molecular and lattice modes is strictly linear, and the sidebands can be understood in terms of Franck–Condon factors between the displaced oscillators, between linearly related normal modes of the ground state and excited state. In this region of the spectrum there is discrepancy in the comparison with experiment of the sideband to zero-phonon line. The fact that the experiment shows less of a sideband than the simulation is somewhat surprising since the simulation assumed identical Cl–Ar potentials in initial and final states.

In the case of the high-energy trajectories, the observed behavior is quite different. The amplitudes in each case (solid lines in Fig. 6) are significantly larger than the shift in minima, indicating that in addition to being displaced, the modes are impulsively driven. Further, the motions are now anharmonic, the results of being driven to amplitudes beyond their harmonic limits. The 12.9 cm^{-1} mode, in its first cycle, shows a frequency significantly higher than the weak excitation case (dashed line). Since the wave vector of the mode is fixed by the lattice dimensions, higher frequency in this case means ultrasonic motion or a shock wave that quickly dissipates. We note that this mode involves center-of-mass motion of Cl_2, and would not be directly excited if the absorption occurred at strictly $T=0$. Not surprisingly, the amplitude in this mode is relatively small, since it is activated by initial thermal noise. The three modes that show the largest amplitudes involve motions directly coupled to the chromophore. The 65.2 and the 46.5 cm^{-1} modes involve the cage atoms around the belt of the Cl_2 molecule, and constitutes local modes that are stiffened by the repulsive wall of the compressed molecule. Both of these modes are initially driven by the attractive part of the Cl_2–Ar potential: when the Cl–Cl bond stretches the Ar atoms are pulled in toward the molecular belt. Attractive coupling will in general produce a large amplitude motion, as observed in these cases. The 24.8 cm^{-1} mode is effectively the cage shell motion, directly driven by the impurity. In contrast, the 58.1 cm^{-1} mode is indirectly excited, through phonon–phonon coupling, and can be seen to buildup amplitude ~ 1.2 ps after initial excitation. That

this mode is mechanically decoupled from the molecule is evident from the displacement vectors shown in the accompanying panel.

The extent and type of phonons excited through dynamical coupling between lattice and chromophobe is highly specific. Inspection of Fig. 1(c) makes it clear that neither the density of states, nor the frequency of the oscillator (energy gap arguments) are sufficient criteria to determine whether particular phonons will be directly or indirectly involved in the dynamics. The specific details are quite sensitive to all parameters of the system: intermolecular potentials, initial temperature, lattice parameters, and structure. Thus it can be hoped that where detailed spectra exist, simulations of the type presented here can be used to ascertain the extent of our understanding of a given system.

V. CONCLUSIONS

We have introduced the method of mixed-order semiclassical molecular dynamics simulations in coherent, Gaussian bases, representation for the expressed purpose of computing quantum time correlation functions in very large systems. We have applied the method rather satisfactorily, to the reproduction and analysis of the vibronic spectrum of Cl_2 isolated in solid Ar, by explicitly simulating the relevant system in its full dimensionality (321 degrees of freedom). As in our earlier method in coordinate representation, key to the success of the implementation is the recognition that for the limited time dynamics involved, quite generally, zeroth-order semiclassical propagators are sufficient to describe the majority of degrees of freedom in condensed media. Moreover, a consistent treatment of super-systems is possible by reserving the computationally intensive second-order propagators to the select degrees of freedom, with selection criteria based on thermal occupation, anharmonicity, or extent of nonlinearity. The numerical algorithm developed for this purpose can treat any number of coordinates by the Herman–Kluk propagator, while treating the others as Heller's frozen Gaussians.

The particular example we considered, the electronic absorption spectrum of Cl_2 in solid Ar is generic of spectra that show zero-phonon lines and phonon sidebands. To our knowledge, the present simulations are the first that allow the dissection of the molecular motions underlying these spectral features. The insights regarding details of dynamical couplings that lead to rather specific and varied types of excitations in this single example should prevail quite generally in the spectroscopy of impurity doped solids.

ACKNOWLEDGMENTS

The support by AFOSR, under a University Research Initiative Grant No. F49620-1-0251, is gratefully acknowledged. The UCI Office of Academic Computing and the Institute for Surface and Interface Science are acknowledged for the allocation of computer resources. We also acknowledge insightful discussions with Professor N. Schwentner regarding this work.

[1] E. J. Heller, Acc. Chem. Res. **14**, 368 (1981).
[2] W. H. Miller, J. Chem. Phys. **53**, 3578 (1970); Adv. Chem. Phys. **25**, 69 (1974).
[3] M. F. Herman and E. Kluk, Chem. Phys. **91**, 27 (1984); E. Kluk, M. F. Herman, and H. L. Davis, J. Chem. Phys. **84**, 333 (1984); M. F. Herman, *ibid.* **85**, 2069 (1986).
[4] E. J. Heller, J. Chem. Phys. **75**, 2933 (1981).
[5] E. J. Heller, J. Chem. Phys. **94**, 2723 (1991).
[6] W. H. Miller, J. Chem. Phys. **95**, 9428 (1991).
[7] M. A. Sepulveda and E. J. Heller, J. Chem. Phys. **101**, 8004, 8016 (1994).
[8] K. G. Kay, J. Chem. Phys. **101**, 2260 (1995); **100**, 4377, 4432 (1994).
[9] A. R. Walton and D. F. Manolopoulos, Chem. Phys. Lett. **244**, 448 (1995); Mol. Phys. **87**, 961 (1996).
[10] B. W. Spath and W. H. Miller, J. Chem. Phys. **104**, 95 (1996); Chem. Phys. Lett. **262**, 484 (1996).
[11] S. Garashchuk and D. J. Tannor, Chem. Phys. Lett. **262**, 477 (1996); S. Garashchuk, F. Grossmann, and D. J. Tannor, J. Chem. Soc. Faraday Trans. **93**, 781 (1997); F. Grossmann, Chem. Phys. Lett. **262**, 470 (1996).
[12] F. Grossmann and E. J. Heller, Chem. Phys. Lett. **241**, 45 (1995); N. T. Maitra and E. J. Heller, Phys. Rev. Lett. **78**, 3035 (1997).
[13] K. G. Kay, J. Chem. Phys. **107**, 2313 (1997).
[14] X. Sun and W. H. Miller, J. Chem. Phys. **106**, 6346 (1997).
[15] G. Stock and M. Thoss, Phys. Rev. Lett. **78**, 578 (1997).
[16] V. S. Batista and W. H. Miller, J. Chem. Phys. (submitted).
[17] J. Cao and G. V. Voth, J. Chem. Phys. **104**, 273 (1996).
[18] X. Sun and W. H. Miller, J. Chem. Phys. **106**, 916 (1997).
[19] M. Ovchinnikov and V. A. Apkarian, J. Chem. Phys. **105**, 10312 (1996).
[20] M. Ovchinnikov and V. A. Apkarian, J. Chem. Phys. **106**, 5775 (1997).
[21] M. L. Brewer, J. S. Hulme, and D. E. Manolopoulos, J. Chem. Phys. **106**, 4832 (1997).
[22] V. E. Bondybey and C. Fletcher, J. Chem. Phys. **64**, 3615 (1976).
[23] J. H. Van Vleck, Proc. Natl. Acad. Sci. USA **14**, 178 (1928).
[24] M. C. Gutzwiller, J. Math. Phys. **8**, 1979 (1967).
[25] G. Herzberg, *Spectra of Diatomic Molecules* (Van Nostrand Reinhold, New York, 1950).
[26] H. Kunz, J. G. McCaffrey, R. Schriever, and N. Schwentner, J. Chem. Phys. **94**, 1039 (1991); J. G. McCaffrey, H. Kunz, and N. Schwentner, *ibid.* **96**, 155 (1992).
[27] R. Alimi, R. B. Gerber, J. G. McCafferey, H. Kunz, and N. Schwentner, Phys. Rev. Lett. **69**, 856 (1992).
[28] *Inert Gases. Potentials, Dynamics, and Energy Transfer in Doped Crystals*, edited by M. L. Klein (Springer-Verlag, Berlin, 1984).
[29] The more common definition of the strength of electron-phonon coupling, *S*, is the logarithmic ratio of intensity in the zero-phonon line to the overall band. See, for example, C. P. Flynn, *Point Defects and Diffusion* (Clarendon, Oxford, 1972), p. 252.
[30] B. L. Grigorenko, A. V. Nemukhin, and V. A. Apkarian, Chem. Phys. **219**, 161 (1997).